

Experimental access to higher-order Zeeman effects by precision spectroscopy of highly charged ions in a Penning trap

D. von Lindenfels

*GSI Helmholtzzentrum für Schwerionenforschung, Planckstrasse 1, 64291 Darmstadt, Germany and
Max-Planck-Institut für Kernphysik, Saupfercheckweg 1, 69117 Heidelberg, Germany*

M. Wiesel

*Institut für Angewandte Physik, Technische Universität Darmstadt, 64289 Darmstadt, Germany and
Physikalisches Institut, Im Neuenheimer Feld 226, 69120 Heidelberg, Germany*

D. A. Glazov and A. V. Volotka

*Department of Physics, St. Petersburg State University, Oulianovskaya 1, Petrodvorets, 198504 St. Petersburg, Russia and
Institut für Theoretische Physik, Technische Universität Dresden, Mommsenstraße 13, 01062 Dresden, Germany*

M. M. Sokolov and V. M. Shabaev

Department of Physics, St. Petersburg State University, Oulianovskaya 1, Petrodvorets, 198504 St. Petersburg, Russia

G. Plunien

Institut für Theoretische Physik, Technische Universität Dresden, Mommsenstraße 13, 01062 Dresden, Germany

W. Quint

*GSI Helmholtzzentrum für Schwerionenforschung, Planckstrasse 1, 64291 Darmstadt, Germany and
Physikalisches Institut, Im Neuenheimer Feld 226, 69120 Heidelberg, Germany*

G. Birkel, A. Martin, and M. Vogel*

Institut für Angewandte Physik, Technische Universität Darmstadt, 64289 Darmstadt, Germany

(Received 19 November 2012; published 15 February 2013)

We present an experimental concept and setup for laser-microwave double-resonance spectroscopy of highly charged ions in a Penning trap. Such spectroscopy allows a highly precise measurement of the Zeeman splittings of fine- and hyperfine-structure levels due to the magnetic field of the trap. We have performed detailed calculations of the Zeeman effect in the framework of quantum electrodynamics of bound states as present in such highly charged ions. We find that apart from the linear Zeeman effect, second- and third-order Zeeman effects also contribute to the splittings on a level of 10^{-4} and 10^{-8} , respectively, and hence are accessible to a determination within the achievable spectroscopic resolution of the ARTEMIS experiment currently in preparation.

DOI: [10.1103/PhysRevA.87.023412](https://doi.org/10.1103/PhysRevA.87.023412)

PACS number(s): 32.60.+i, 42.62.Fi, 78.70.Gq, 37.10.Ty

I. INTRODUCTION

Ever since the discovery of a quadratic contribution to the Zeeman effect by Jenkins and Segré in the 1930s [1,2], there have been numerous studies both experimental and theoretical of higher-order Zeeman contributions in atoms, molecules, and singly charged ions in laboratory magnetic fields (see, for example, [3–6]). The high magnetic field strengths present in astronomical objects have given impetus to corresponding studies in observational astronomy [7–11], identifying a quadratic Zeeman effect in abundant species like hydrogen and helium. Although highly charged ions are both abundant in the universe and readily accessible in laboratories, to our knowledge, no higher-order Zeeman effect in highly charged ions has been observed so far.

In highly charged ions of a given charge state, the electronic energy level splittings depend strongly on the nuclear charge

Z . For one-electron ions (i.e., hydrogenlike ions) the energy splitting is proportional to Z^2 for principal transitions, to Z^3 for hyperfine-structure transitions, and to Z^4 for fine-structure transitions. In other few-electron ions the scaling is very similar [12,13]. Since in the hydrogen atom principal transitions are typically at a few eV, the scaling with Z^2 shifts these transitions far into the XUV and x-ray regime for heavier hydrogenlike ions, and thus out of the reach of studies like the present one.

In an external magnetic field, the Zeeman effect lifts the degeneracy of energies within fine- and hyperfine-structure levels. For highly charged ions in magnetic fields of a few tesla strength as typical for Penning trap operation, the corresponding Zeeman splitting is well within the microwave domain and thus accessible for precision spectroscopy. In addition, in fine- and hyperfine-structure transitions, the strong scaling with Z eventually shifts the corresponding energies into the laser-accessible region and thus makes them available for precision optical spectroscopy [14].

We are currently setting up a laser-microwave double-resonance spectroscopy experiment with highly charged ions

*m.vogel@gsi.de

in a Penning trap, which combines precise spectroscopy of both optical transitions and microwave Zeeman splittings [15,16]. The experiment aims at spectroscopic precision measurements of such energy level splittings and magnetic moments of bound electrons on the ppb level of accuracy and better. At the same time, it allows access to the nuclear magnetic moment in the absence of diamagnetic shielding [15,17]. For first tests within the AsymmetRiC Trap for the measurement of Electron Magnetic moments in IonS (ARTEMIS) experiment, the $^{40}\text{Ar}^{13+}$ ion has been chosen. It has a spinless nucleus, such that only a fine structure is present. Similar measurements in hyperfine structures are to be performed with ions of higher charge states such as, for example, $^{207}\text{Pb}^{81+}$ and $^{209}\text{Bi}^{82+}$ as available to ARTEMIS within the framework of the HITRAP facility [18] at GSI, Germany.

We have performed detailed relativistic calculations of the Zeeman effect in boronlike ions such as Ar^{13+} . These calculations show that at the ppb level of experimental accuracy, higher-order effects play a significant role and need to be accounted for. In turn, precision spectroscopy of highly charged ions allows a measurement of these higher-order contributions to the Zeeman effect.

II. CALCULATION OF THE ZEEMAN EFFECT

We consider a five-electron argon ion in the ground $[(1s)^2(2s)^22p]^2P_{1/2}$ and in the first excited $[(1s)^2(2s)^22p]^2P_{3/2}$ states. The fine-structure interval between these levels has previously been studied [19–22], as well as the corresponding magnetic dipole transition rate [23–26]. An external magnetic field splits levels with different angular momentum projection onto the direction of the field. While this splitting is equidistant in the first-order approximation, the nonlinear magnetic field effects disturb this symmetry. The corresponding level structure is schematically depicted in Fig. 1.

The Zeeman shift of each level can be evaluated within perturbation theory,

$$E_A(B) = E_A^{(0)} + \Delta E_A^{(1)}(B) + \Delta E_A^{(2)}(B) + \Delta E_A^{(3)}(B) + \dots, \quad (1)$$

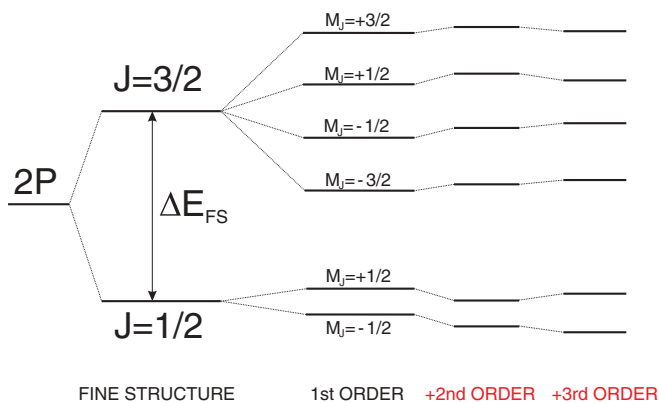


FIG. 1. (Color online) Level scheme of the 2^2P_J states of boronlike argon Ar^{13+} in an external magnetic field with higher-order contributions to the Zeeman effect (not true to scale).

where $|A\rangle = |J, M_J\rangle$ is the 2^2P_J state with total angular momentum J and its projection M_J . In the following, the quantities which do not depend on M_J (e.g., the energy in the absence of magnetic field, $E_A^{(0)}$) are labeled with J only. Each term of the perturbation expansion is proportional to the magnetic field strength to the corresponding power, $\Delta E_A^{(n)}(B) \sim B^n$. The first-order term is directly related to the g_J factor by

$$\Delta E_A^{(1)}(B) = g_J M_J \mu_B B, \quad (2)$$

where μ_B is the Bohr magneton. The Dirac equation for the valence $|a\rangle = |2p\rangle$ electron is an appropriate zeroth approximation to find $\Delta E_A^{(1)}(B)$ as

$$\Delta E_A^{(1)}(B) = \langle a | V_m | a \rangle, \quad (3)$$

where the operator

$$V_m = \frac{|e|\hbar}{2} [\mathbf{r} \times \boldsymbol{\alpha}] \cdot \mathbf{B} \quad (4)$$

represents the interaction with the external homogeneous magnetic field \mathbf{B} . For the Coulomb potential of a pointlike nucleus, one finds

$$g_{1/2} = \frac{2}{3} \left[\sqrt{2[1 + \sqrt{1 - (\alpha Z)^2}] - 1} \right] \\ = \frac{2}{3} - \frac{1}{6}(\alpha Z)^2 - \frac{5}{96}(\alpha Z)^4 - \dots, \quad (5)$$

$$g_{3/2} = \frac{4}{15} \left[2\sqrt{4 - (\alpha Z)^2} + 1 \right] \\ = \frac{4}{3} - \frac{2}{15}(\alpha Z)^2 - \frac{1}{120}(\alpha Z)^4 - \dots. \quad (6)$$

The interelectronic interaction, quantum electrodynamical, and nuclear effects give rise to corrections to these values. Evaluation of the g_J factors of the $2^2P_{1/2}$ and $2^2P_{3/2}$ states of boronlike argon in Ref. [21] yielded $g_{1/2} = 0.663\,65$ and $g_{3/2} = 1.332\,28$. These values include the one-loop QED term and the interelectronic interaction correction. The latter was calculated within the configuration-interaction method with the basis functions derived from the Dirac-Fock and Dirac-Fock-Sturm equations. The contribution of the negative-energy states, which is crucially important for the Zeeman effect, was taken into account within perturbation theory. Recently, the g_J factors have been improved to $g_{1/2} = 0.663\,647(1)$ and $g_{3/2} = 1.332\,285(3)$ [27]. In comparison to those from Ref. [21], these include the $1/Z$ term of the interelectronic interaction, evaluated within the QED approach, the screening correction to the one-loop self-energy term, and the nuclear recoil effect.

The second- and third-order terms in the Zeeman splitting can be presented in the following form:

$$\Delta E_A^{(2)}(B) = g_J^{(2)}(M_J)(\mu_B B)^2/E_0, \quad (7)$$

$$\Delta E_A^{(3)}(B) = g_J^{(3)}(M_J)(\mu_B B)^3/E_0^2, \quad (8)$$

where $E_0 = mc^2$ is the electron rest energy, while $g_J^{(2)}$ and $g_J^{(3)}$ are dimensionless coefficients. Their dependence on M_J is not as simple as for the first-order effect; however, they obey the symmetry relations $g_J^{(2)}(-M_J) = g_J^{(2)}(M_J)$ and $g_J^{(3)}(-M_J) = -g_J^{(3)}(M_J)$.

The leading-order contributions to $\Delta E_A^{(2)}$ and $\Delta E_A^{(3)}$ can be calculated according to the formulas

$$\Delta E_A^{(2)}(B) = \sum_n' \frac{\langle a|V_m|n\rangle\langle n|V_m|a\rangle}{\varepsilon_a - \varepsilon_n}, \quad (9)$$

$$\begin{aligned} \Delta E_A^{(3)}(B) = & \sum_{n_1, n_2}' \frac{\langle a|V_m|n_1\rangle\langle n_1|V_m|n_2\rangle\langle n_2|V_m|a\rangle}{(\varepsilon_a - \varepsilon_{n_1})(\varepsilon_a - \varepsilon_{n_2})} \\ & - \sum_n' \frac{\langle a|V_m|n\rangle\langle n|V_m|a\rangle}{(\varepsilon_a - \varepsilon_n)^2} \langle a|V_m|a\rangle, \end{aligned} \quad (10)$$

where the summations run over the complete Dirac spectrum, excluding the reference state $|a\rangle$. It is absolutely important to take into account the negative-energy states in Eqs. (9) and (10), since their contribution is not small as compared to that of the positive-energy states even for low nuclear charge Z (nonrelativistic limit). In particular, in hydrogenlike ($|a\rangle = |1s\rangle$) and lithiumlike ($|a\rangle = |2s\rangle$) ions the negative continuum delivers a dominant part of these higher-order terms. However, in magnetic fields of several tesla, their magnitudes appear to be far below the experimental precision. For example, the g_J factors of hydrogen- and lithiumlike silicon ions have been measured recently with ppb accuracy at a magnetic field of 3.76 T [28,29]. In these cases, the relative contribution of the third-order effect $|\Delta E^{(3)}/\Delta E^{(1)}|$ is 0.05×10^{-15} and 0.8×10^{-15} , respectively. Although the quadratic shift is not so small, $|\Delta E^{(2)}/\Delta E^{(1)}| = 0.7 \times 10^{-6}$ for lithiumlike silicon, it does not affect the ground-state Zeeman splitting for states with $J = 1/2$. Just as in the present case (see Fig. 1), both sublevels are shifted by the same amount, which cancels in the transition frequency.

In contrast, in boronlike ions the higher-order effects appear to be well observable. This is due to the relatively small fine-structure interval between the states $2p_{1/2}$ and $2p_{3/2}$. Below we consider the Zeeman shifts for both of these states. While $|a\rangle = |2p_{1/2}\rangle, |2p_{3/2}\rangle$ denotes the reference state, $|b\rangle = |2p_{3/2}\rangle, |2p_{1/2}\rangle$ denotes the other state of these two. It has been verified by rigorous calculations that the contribution of the fine-structure partner $|b\rangle$ in Eqs. (9) and (10) is dominant in the case of $M_J = \pm 1/2$. Accordingly, the summations can be restricted to $|n\rangle = |n_1\rangle = |n_2\rangle = |b\rangle$ to yield the estimations

$$\Delta E_A^{(2)}(B) \approx \frac{|\langle a|V_m|b\rangle|^2}{\varepsilon_a - \varepsilon_b}, \quad (11)$$

$$\Delta E_A^{(3)}(B) \approx \frac{|\langle a|V_m|b\rangle|^2}{(\varepsilon_a - \varepsilon_b)^2} (\langle b|V_m|b\rangle - \langle a|V_m|a\rangle). \quad (12)$$

Equation (11) shows that $\Delta E_A^{(2)}$ is approximately of the same magnitude and of opposite sign for the two considered states. Equation (12) shows that the same holds for $\Delta E_A^{(3)}$. Even more simplified order-of-magnitude estimations of these effects are valid in the present case,

$$\frac{\Delta E_A^{(2)}(B)}{\Delta E_A^{(1)}(B)} \sim \frac{\Delta E_A^{(1)}(B)}{\Delta E_{\text{FS}}} \sim 10^{-4}, \quad (13)$$

$$\frac{\Delta E_A^{(3)}(B)}{\Delta E_A^{(1)}(B)} \sim \left(\frac{\Delta E_A^{(1)}(B)}{\Delta E_{\text{FS}}} \right)^2 \sim 10^{-8}, \quad (14)$$

where $\Delta E_{\text{FS}} = E_{3/2}^{(0)} - E_{1/2}^{(0)}$ is the fine-structure interval. Please note, however, that Eqs. (11)–(14) are justified by rigorous calculations according to Eqs. (9) and (10) for the

TABLE I. $g_J^{(2)}$ and $g_J^{(3)}$ factors [Eqs. (7) and (8)] and the corresponding coefficients $a_J^{(2)}$ and $a_J^{(3)}$ [Eqs. (17) and (18)] for boronlike argon.

J, M_J	$g_J^{(2)}(M_J)$	$a_J^{(2)}(M_J)$ (kHz/T ²)	$g_J^{(3)}(M_J)$	$a_J^{(3)}(M_J)$ (Hz/T ³)
$3/2, \pm 3/2$	0.95×10^3	1.5	$\mp 5.7 \times 10^3$	$\mp 1.0 \times 10^{-6}$
$3/2, \pm 1/2$	41.0×10^3	65.1	$\mp 2.5 \times 10^9$	∓ 0.45
$1/2, \pm 1/2$	-39.5×10^3	-62.6	$\pm 2.5 \times 10^9$	± 0.45

$2p_{1/2}$ and $2p_{3/2}$ states and are not necessarily valid in other cases.

We have performed the calculations according to Eqs. (9) and (10) within the dual-kinetic-balance (DKB) approach [30] with the basis functions constructed from B splines [31]. Several effective screening potentials, which partly take into account the interelectronic-interaction effects (see, e.g., [32–35]), have been employed to estimate the uncertainty of the results. As one can see from Eqs. (9) and (10) the higher-order effects are highly sensitive to the fine-structure energy splitting ΔE_{FS} , which is significantly affected by the interelectronic-interaction and QED effects. Therefore, instead of the value of ΔE_{FS} provided by the Dirac equation with the screening potential we employed the best up-to-date theoretical value from Ref. [20], which is in perfect agreement with the experimental one [22]. Finally, the values for different screening potentials have been averaged. The results for $g_J^{(2)}$ and $g_J^{(3)}$ are presented in Table I. They are in agreement with the values obtained by Tupitsyn within the large-scale configuration-interaction Dirac-Fock-Sturm method [36]. We estimate the uncertainty of the values obtained roughly as 10%. Rigorous evaluation of the correlation effects beyond the screening-potential approximation is needed. QED and nuclear recoil effects have to be taken into account as well.

The energies of the Zeeman sublevels including the linear and nonlinear effects can be written as

$$E_A(B) = E_J^{(0)} + h \sum_{i=1}^{\infty} a_J^{(i)}(M_J) B^i. \quad (15)$$

The coefficients $a_J^{(i)}(M_J)$ are directly related to the g_J , $g_J^{(2)}$, and $g_J^{(3)}$ factors, defined by Eqs. (2), (7), and (8),

$$ha_J^{(1)}(M_J) = g_J M_J \mu_B, \quad (16)$$

$$ha_J^{(2)}(M_J) = g_J^{(2)}(M_J) \mu_B^2 / (mc^2), \quad (17)$$

$$ha_J^{(3)}(M_J) = g_J^{(3)}(M_J) \mu_B^3 / (mc^2)^2. \quad (18)$$

The values of the coefficients $a_J^{(2)}$ and $a_J^{(3)}$ are presented in Table I along with $g_J^{(2)}$ and $g_J^{(3)}$.

Table II shows the first-, second-, and third-order contributions to the Zeeman shift of individual levels in boronlike argon in a magnetic field of 7 T. The linear effect separates the two ground-state ($2^2P_{1/2}$) levels by about 65 GHz and the four excited-state ($2^2P_{3/2}$) levels by about 130 GHz. The quadratic effect shifts both $|1/2, \pm 1/2\rangle$ levels down and the two $|3/2, \pm 1/2\rangle$ levels up by about 3 MHz. This effect is exactly independent of the sign of M_J , while the shifts for $J = 1/2$ and $J = 3/2$ are slightly different. The $|3/2, \pm 3/2\rangle$

TABLE II. Contributions to the Zeeman energy shifts for boron-like argon at 7 T. First, second, and third orders in the magnetic field are presented in terms of the frequencies $\Delta E/h$.

J, M_J	$\Delta E_A^{(1)}/h$ (GHz)	$\Delta E_A^{(2)}/h$ (MHz)	$\Delta E_A^{(3)}/h$ (Hz)
3/2, +3/2	195.793	0.074	-0.00035
3/2, +1/2	65.264	3.19	-153
3/2, -1/2	-65.264	3.19	153
3/2, -3/2	-195.793	0.074	0.00035
1/2, +1/2	32.5100	-3.07	153
1/2, -1/2	-32.5100	-3.07	-153

levels are shifted up by 74 kHz. So the second-order effect contributes to the transition frequencies ν_a and ν_c , which are introduced in the next section (see also Fig. 2). The cubic effect increases the splitting between the ground-state levels by about 306 Hz, thus simulating a contribution of 3×10^{-9} to $g_{1/2}$. The splitting between the $|3/2, \pm 1/2\rangle$ levels is decreased by approximately the same value.

III. DOUBLE-RESONANCE SPECTROSCOPY

A. General concept

The technique of laser-microwave double-resonance spectroscopy has been applied in experiments with singly charged ions [37–39]. Presently, the concept can be exemplified by Fig. 2. It shows all six components of the Zeeman-split magnetic dipole transition between the two fine-structure states of a P electron. Neighboring lines are all separated by about the same frequency difference, because the upper-state level spacing is about twice as large as that in the lower state. If an ion gets excited by the most redshifted frequencies (ν_1 or ν_2), the angular momentum projection is lowered

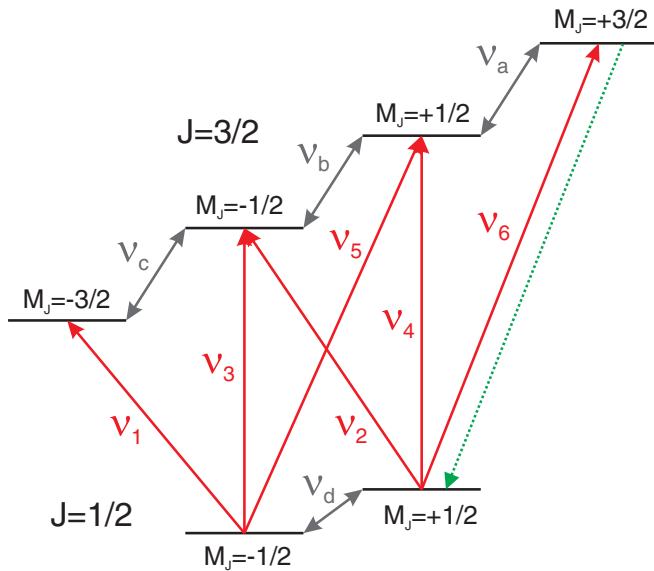


FIG. 2. (Color online) Spectroscopy of the $2^2P_{1/2} - 2^2P_{3/2}$ fine-structure transition, as in a boronlike argon ion Ar^{13+} , with Zeeman effect. The level scheme (not true to scale) and all magnetic dipole transitions are shown. Solid arrows indicate excitation by laser photons, while dotted arrows are spontaneous decays. Gray double arrows represent microwave transitions.

by 1. The fluorescence light corresponding to these transitions is emitted mainly along the quantization axis with circular polarization. Yet a fraction can also be detected under radial observation. This component is polarized parallel to the axis. The frequencies ν_3 and ν_4 are the closest to the field-free frequency. The corresponding transitions preserve the angular momentum projection and can be observed only radially and with perpendicular polarization. Excitation with the most blueshifted lines at ν_5 or ν_6 increases the angular momentum projection. The emitted fluorescence follows the same distribution as in the case of ν_1 or ν_2 , but has opposite helicity.

The basic idea of double-resonance spectroscopy is contained in the following example: A closed optical cycle between the extremal states $|1/2, +1/2\rangle$ and $|3/2, +3/2\rangle$ is driven resonantly by a laser at frequency ν_6 . The corresponding fluorescence light (dotted arrow) is observed continuously. In the absence of microwave radiation the fluorescence light intensity is constant. When either of the microwave transitions at ν_a or ν_d is driven resonantly, population is withdrawn from the optical cycle and the amount of fluorescence light is reduced. Hence, the optical signal indicates when the desired microwave transition is resonantly driven, yielding the desired Zeeman transition frequency. A detailed discussion of the applicability of this concept in different level-scheme situations is given in [15]. Note that all Zeeman sublevels can be addressed individually since their separation is much larger than the laser width and the Doppler widths of the optical transitions.

B. Application to an optical P doublet

In the present application, the optical transition is a ground-state fine-structure transition in a highly charged ion, while the microwave transition occurs between corresponding Zeeman sub-levels. Both are magnetic dipole ($M1$) transitions with accordingly long lifetimes of the upper levels. By laser-microwave double-resonance spectroscopy, the Zeeman sublevel splittings can be measured with high accuracy. This yields access to differences of the coefficients defined in Sec. II rather than to the values themselves. Therefore we abbreviate:

$$a_i \equiv a_{1/2}^{(i)}(1/2) - a_{1/2}^{(i)}(-1/2), \quad i = 1, 3,$$

$$b_i \equiv a_{3/2}^{(i)}(3/2) - a_{3/2}^{(i)}(1/2), \quad i = 1, 2, 3,$$

$$b'_3 \equiv a_{3/2}^{(3)}(3/2).$$

Due to the tiny value of $b'_3 B^3 < 1$ mHz, we cannot distinguish b_3 from $-a_{3/2}^{(3)}(1/2)$.

The upper-level Zeeman splitting is of particular interest, because here the quadratic shift actually has a measurable effect on the Larmor frequencies. We name the three frequencies ν_a , ν_b , and ν_c , while the ground-state Larmor frequency is ν_d , as denoted in Fig. 2.

The combination of particular frequencies can be used to disentangle the different orders:

$$\begin{aligned} \nu_d &= a_1 B & + a_3 B^3, \\ \nu_a + \nu_c &= 2b_1 B & + 2b_3 B^3, \\ \nu_a - \nu_c &= & 2b_2 B^2, \\ \nu_a + \nu_b + \nu_c &= 3b_1 B & + 2b'_3 B^3, \\ \nu_a + \nu_c - 2\nu_b &= & 6b_3 B^3 - 4b'_3 B^3. \end{aligned}$$

Neglecting $b_3 B^3$, we can immediately derive b_1, b_2, b_3 from the latter equations, provided the magnetic field strength has been measured with corresponding accuracy. In the lower state, the quadratic effect cancels. This is different for the cubic order: So far, we have to use the theoretical prediction for a_3 in order to determine a_1 . A similar procedure would yield b_1 in the case of an insufficient ν_b measurement:

$$g_{1/2} \frac{\mu_B}{h} \equiv a_1 = \frac{1}{B} (\nu_d - a_3 B^3),$$

$$g_{3/2} \frac{\mu_B}{h} \equiv b_1 = \frac{1}{B} \left(\frac{\nu_a + \nu_c}{2} - b_3 B^3 \right).$$

Under these conditions, we can imagine several different spectroscopic options. All involve blue laser radiation ($\lambda \approx 441$ nm) and a microwave field with at least one of the aforementioned frequencies. Therefore, the term “double resonance” may be extended to “triple” or even “quadruple” resonance. In any case, the optical spectroscopy serves to prepare or detect population in specific Zeeman states and thus allows us to see whether the microwave frequency is at resonance with the transition of interest. The set frequency together with the measured response of the ions is used to determine the Larmor frequency. In the following, we will explain the most useful and viable concept and just briefly mention variations.

For any microwave scan, we start with a spectrally broad signal (statistical or a Landau-Zener sweep) and iteratively lower the width. This can be performed by an external modulation of the output frequency of the microwave generator. In addition, the modulation technique allows us to apply multiple sharp frequencies at once.

The ratio of g_J values in the respective states is close to 2, namely, 2.007. The frequencies to be generated before multiplication are, according to the current theoretical estimation,

$$\nu_a/8 = 16.323 \text{ GHz}, \quad \nu_b/8 = 16.323 \text{ GHz},$$

$$\nu_c/8 = 16.324 \text{ GHz}, \quad \nu_d/4 = 16.262 \text{ GHz}.$$

These frequencies are well within the few-percent spectral acceptance of an active quadrupler for ν_d . We use an additional doubling stage for the upper-level Larmor frequencies ν_a , ν_b , and ν_c . Thus we can address several upper-level Larmor transitions simultaneously, namely, by nonlinear mixing of close-lying fundamental frequencies.

The relatively long lifetime of 9.6 ms has two benefits: First, it allows a temporal separation of excitation and detection, and, second, the microwaves have enough time to stimulate transitions between the excited-level substates in the upper fine-structure level. Anyway, the precision of the upper-level Larmor frequencies is limited by the natural linewidth of about 100 Hz.

1. Separation of the linear and quadratic effects

The $|1/2, +1/2\rangle$ population is probed by a laser at frequency ν_6 (see Fig. 3). This drives the closed transition to the $|3/2, +3/2\rangle$ sublevel. If the laser is resonant, we repeatedly see fluorescence photons from roughly half of all ions. When the microwave field is resonant with the upper-level Larmor frequency, the cycle will be disturbed. An additional decay channel is opened that leads via $|3/2, +1/2\rangle$ either back or

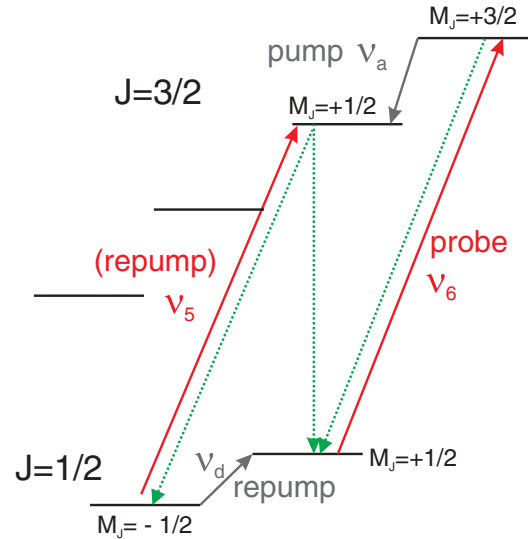


FIG. 3. (Color online) Probe spectroscopy in the Zeeman-split fine-structure doublet. Solid arrows indicate the saturated probing and, optionally, pumping laser photons, while dotted arrows are spontaneous decays. Gray arrows represent microwave-stimulated transitions.

into the dark state $|1/2, -1/2\rangle$. Therefore, after a pumping period with length depending on the respective intensities and temporal overlap of the exciting fields, the fluorescence signal will vanish.

A microwave in resonance with ν_d repumps at least half of the ions (the accurate number again depends on the relative intensities) back to the bright state. This is a reversible process. We can measure pumping and repumping efficiencies over and over and arrive at a count rate that depends on the frequencies only and not on the history of irradiation. This procedure defines a line shape. However, the scan of a single parameter requires the others to be kept sufficiently stable. At least the ground-state repumping can be done efficiently by sweeping over the resonance. This intensifies the signal for finding the upper-level Larmor resonance. A more general concept is to monitor the yielded fluorescence intensity as a function of all three frequencies. The multiresonance condition will be represented as a saddle point in this map.

Simultaneous or alternating irradiation with an additional repumping laser beam would facilitate the measurement. Unfortunately, this is currently not feasible, because the frequencies ν_5 and ν_6 are separated by 65 GHz. There are no modulators producing such far-distant sidebands, and a second light source would be needed. A weaker magnetic field or smaller g_J factor would bring this method back into play.

This method may be inverted in the following sense: The microwave frequency ν_a is replaced by ν_c , while the laser frequency is reduced by 325 GHz from ν_6 to ν_1 . Given the spontaneous transition rate between adjacent Zeeman levels of the order of 10^{-10} s^{-1} , the inverse processes are equivalent to the original ones.

2. Separation of the cubic effect

a. Saturated excitation. According to the above arithmetic, many Zeeman coefficients can be derived already from the

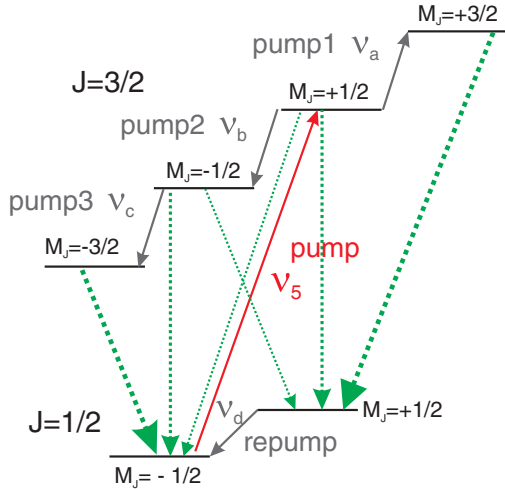


FIG. 4. (Color online) Pump spectroscopy in the Zeeman-split fine-structure doublet. Solid arrows indicate the saturated pumping laser photons, while dotted arrows are spontaneous decays. Projection-conserving decays of the states $|3/2, +1/2\rangle$ and $|3/2, -1/2\rangle$ are preferred. Gray arrows represent microwave-stimulated transitions.

frequencies discussed so far. To improve the coefficient b_1 or to get any reliable information about the cubic order, it is desirable to measure ν_b as well.

To this end, we look into a method that uses laser pumping instead of probing. This is illustrated in Fig. 4: For instance, we depopulate the sublevel $|1/2, -1/2\rangle$ by exciting ions in this state to the $|3/2, +1/2\rangle$ state with the pump frequency ν_5 . This level can decay back to the original state or into the dark state $|1/2, +1/2\rangle$. After a few cycles, the fluorescence will vanish. Additional irradiation of a microwave at the lower-level resonant frequency will repump ions to the state $|1/2, -1/2\rangle$. A continuous fluorescence signal is a signature of both waves being in resonance with the corresponding transition.

As a side effect, this would even improve the two-dimensional line shape (the map of the fluorescence intensity versus the two frequencies of the laser and the microwave): The maximum of this can be determined with higher accuracy than the above-mentioned saddle point. On the downside, the detectable fluorescence intensity suffers compared to the probe transition, which is a pure $|\Delta M_J| = 1$ transition with enhanced emission in the axial direction.

This argument leads back to the original chain of thought: We can identify specific substates by the directional characteristic and branching of different decay modes. If we drive the upper-level Larmor transition from the $|3/2, +1/2\rangle$ state to $|3/2, +3/2\rangle$, ions will decay in the projection-changing channel only. This should lead to a more intense optical signal. However, for this interference-prone signature, it is necessary to have excellent control of the population distribution in the ground-state sublevels. If the drive works efficiently, we see yet another effect: The pumping ends faster than before, because $|3/2, +1/2\rangle$ can still decay into the bright state.

This study of pumping efficiencies works in a similar way for the transition from $|3/2, +1/2\rangle$ to $|3/2, -1/2\rangle$. The decay branching of the $|3/2, +1/2\rangle$ level is 2:1 in favor of $|1/2, +1/2\rangle$, while the total decay rate is the same as of the

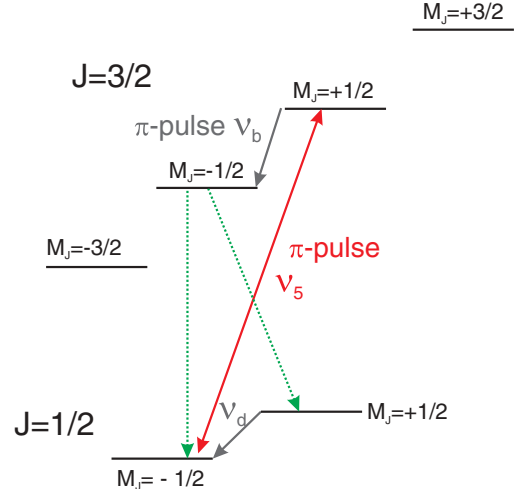


FIG. 5. (Color online) Rabi spectroscopy in the Zeeman-split fine-structure doublet. The solid double arrow indicates coherent excitation or deexcitation by laser photons, while dotted arrows are spontaneous decays. Gray arrows represent microwave-stimulated transitions.

$|3/2, +3/2\rangle$ state. Now we can distinguish $|3/2, +1/2\rangle$ from $|3/2, -1/2\rangle$ in a spectroscopic experiment: After excitation from $|1/2, -1/2\rangle$ to $|3/2, +1/2\rangle$, ions usually come back with a probability of $1/3$, while the remaining ions fall into the dark state $|1/2, +1/2\rangle$. A resonant microwave stimulation of the $|3/2, +1/2\rangle \leftrightarrow |3/2, -1/2\rangle$ transition enhances the decay into the original state up to a probability of $2/3$, which is a factor of 2 in pumping efficiency. An additional drive of the $|3/2, -1/2\rangle \leftrightarrow |3/2, -3/2\rangle$ transition could theoretically prevent the ions from decaying into the dark state at all.

b. Coherent excitation. An alternative approach to determine the transition frequency ν_b can be based on Rabi spectroscopy [40], as shown in Fig. 5. With laser light of the frequency ν_5 , resonant with the transition $|1/2, -1/2\rangle \leftrightarrow |3/2, +1/2\rangle$, it is possible to drive Rabi oscillations between both states. The preparation scheme starts with all population in $|1/2, -1/2\rangle$. An applied laser light pulse with area π (π pulse) leads to a complete population transfer to the state $|3/2, +1/2\rangle$. From there, a microwave pulse at a frequency close to ν_b pumps the ions to $|3/2, -1/2\rangle$ with an efficiency depending on power, frequency, and duration. The remaining population in $|3/2, +1/2\rangle$ will be transferred back to the initial $|1/2, -1/2\rangle$ state with a second laser light π pulse, yielding no detectable light. In the case of a resonant microwave frequency all particles are in the state $|3/2, -1/2\rangle$, and the last light pulse cannot deexcite the ions. They will instead decay spontaneously in the subsequent milliseconds and can with a certain detection efficiency be seen by the detector. When the frequency of the microwave has been detuned compared to the transition frequency ν_b , no or less fluorescence will be visible. After several cycles, the ions will get pumped into the state $|1/2, +1/2\rangle$. Therefore we introduce an additional signature: The population in this dark state can be monitored with a second laser at frequency ν_6 (probe laser). This drives the closed transition $|1/2, +1/2\rangle \leftrightarrow |3/2, +3/2\rangle$ and produces fluorescence photons. A microwave pulse at the lower-level Larmor frequency ν_d will prepare the initial state again.

IV. EXPERIMENTAL SETUP

A. Magnet

The main components of the experimental setup including the Penning trap itself are surrounded by a vertical room-temperature open-bore magnet (see Fig. 6). It produces the magnetic field which confines the ions and causes the Zeeman splitting. The maximum field strength is 7 T, and the central field region is located at the trap center and has a measured homogeneity of 0.14 ppm over the central volume of 1 cm^3 .

The trap setup is inserted into the 160-mm-diameter magnet bore from the top and represents a shielded cryostat which employs a pulse-tube cryocooler, to which the Penning trap and the cryoelectronic components are attached. The cryostat is a low-vibration pulse-tube cooler with two thermal stages. The first stage has 40 W cooling power at 45 K and maintains the temperature of the radiation shield; the second stage inside the radiation shield has 1 W cooling power at 4.2 K and keeps the trap and its electronics at liquid-helium temperature. Several aspects of this setup have already been described in [16,41]. The working principle of in-trap ion production and transfer is similar to that in [42].

B. Trap

Penning trap designs and properties as relevant for the present experiment have been discussed in great depth, for example, in [14,43–45]. Briefly, in the present experiment, the combination of the vertical homogeneous magnetic field of

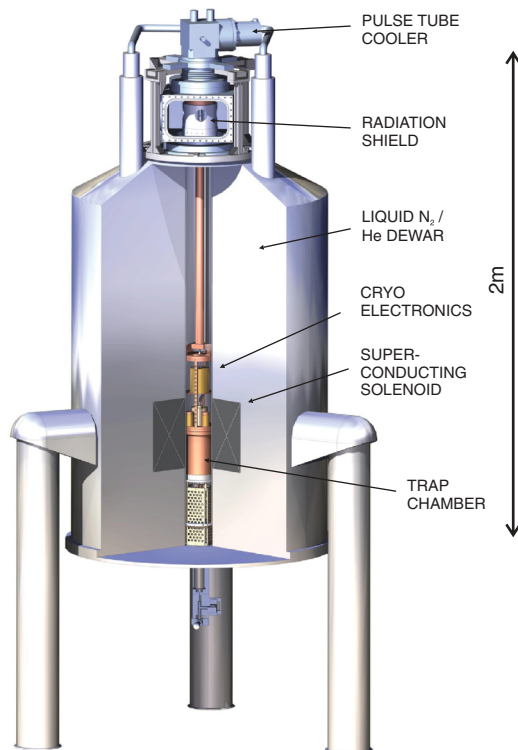


FIG. 6. (Color online) Schematic drawing of the setup. The superconducting magnet has been cut to allow a view of the trap and related components inside the room-temperature bore.

7 T strength with a harmonic electrostatic potential created by appropriate voltages applied to the trap electrodes confines ions close to the trap center in all three dimensions. In the absence of imperfections, each ion performs an oscillatory motion consisting of three eigenmotions, which can be manipulated individually [46,47]. The main manipulation techniques here are cooling of the ion motion and compression of the stored ion cloud, as will be discussed below.

The trap is a stack of cylindrical electrodes as shown in Fig. 7. It consists of a spectroscopy part on the upper end and of an ion production part below. This part features a cold gas source and a cold electron source (field emission point) and can be operated like a miniature electron-beam ion source (EBIS) for in-trap production of highly charged gas ions. To that end, cold electrons are accelerated towards the spectroscopy trap and deflected back and thus oscillate through the region where gas can be injected under well-defined conditions [16,41]. This leads to charge breeding by electron-impact ionization of gas atoms and ions. The electron energy can be adjusted to any value up to about 2.5 keV, the optimum production energy for Ar^{13+} under our conditions has been found to be 1855 eV. To this end, we have performed simulations using the CBSIM software package [41]. The evolution of charge states

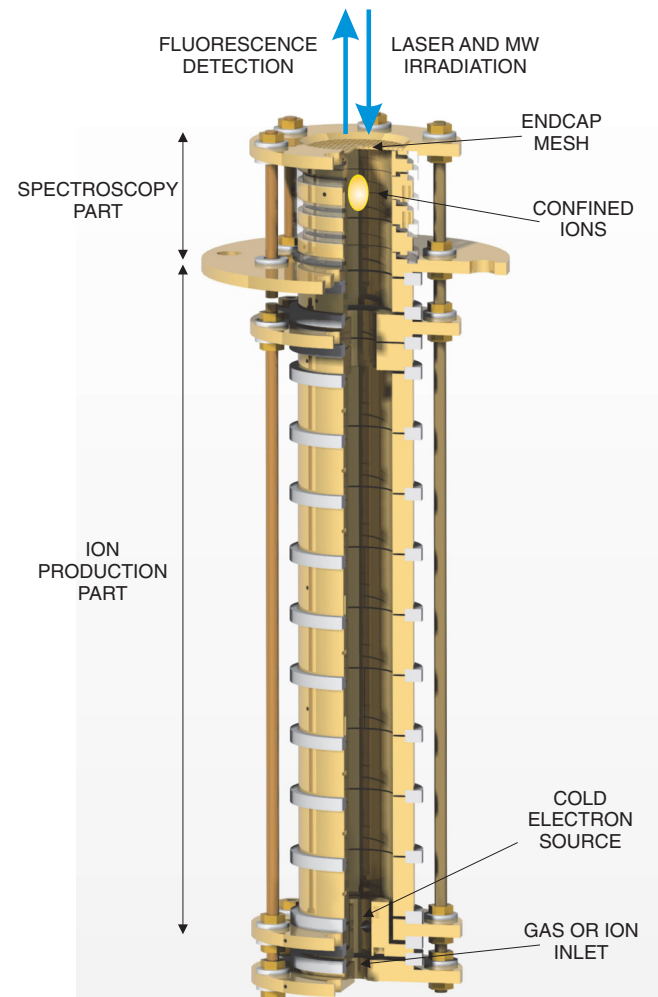


FIG. 7. (Color online) Schematic drawing of the trap. A cut has been applied for presentation of the trap interior.

is monitored by real-time Fourier-transform ion cyclotron resonance mass spectrometry [48]. The ion species of interest is selected by resonant ejection of all unwanted ions [49] and then transported to the spectroscopy trap by appropriate switching of electrode voltages.

Alternatively, the trap can be used for dynamic capture and storage of externally produced ions, for example from an electron-beam ion source or from the HITRAP facility at GSI, Germany [18]. In this mode of operation also, the ions are prepared in the production part of the trap and then transferred to the spectroscopy part for measurements. After loading of the trap with ions, cooling of the ion motion is achieved by resistive cooling [50] using a tuned circuit attached to the split correction electrode of the spectroscopy trap. When the resonance frequency of the circuit is tuned to the ion oscillation frequency (in the first experiments we are mainly interested in cooling of the axial motion), energy from that ion motion is dissipated into the cryogenic surroundings, thus cooling the motion, i.e., reducing its energy and therefore its oscillation amplitude. Such resistive cooling to an equivalent of about 4 K reduces the relative Doppler width of the 441 nm optical transition to about 2×10^{-7} . The same technique is used for a nondestructive measurement of ion oscillation frequencies by so-called “electronic pickup” [50].

In the spectroscopy trap, the ions are confined close to the upper end cap such that fluorescence collection takes place at a comparatively large solid angle through a partially transparent mesh on top of that electrode. The excitation laser light and microwaves are guided into the trap from the top as well.

The ring electrode is split into four equal segments such that a rotating dipole field can be irradiated into the trap center. This allows the application of the “rotating wall” technique for radial compression and shaping [51] of the ion cloud.

C. Laser, microwaves, and detection

The optical transitions with frequencies ν_1 to ν_6 of Fig. 2 at a wavelength of 441.3 nm will be excited by the radiation of a diode laser (TOPTICA DL 100 pro) with an output power of 17 mW and an overall tuning range of 6.4 nm. The manufacturer specifies the spectral width to approximately 1 MHz, which is sufficient to excite the transitions of interest selectively and is narrow enough to resolve the estimated Doppler broadening of 150 MHz. The mode-hop-free tuning range is 22 GHz, easing the search for the transition frequency, which is known within an uncertainty of about 400 MHz [22]. On the other hand, to switch between two or more of the six transition frequencies, manual tuning of the laser frequencies is required. Calibration of the laser frequency will be achieved by Doppler-free saturation spectroscopy on molecular tellurium vapor $^{130}\text{Te}_2$. Tellurium has a mapped set of resonance lines in the visible spectrum, especially in the blue. The “tellurium atlas” [52] contains a series of lines which are between 2.7 and 38 GHz separated from the assumed Ar^{13+} transitions. As acousto-optic, electro-optic, or sideband modulation might not be sufficient to bridge the frequency gap to a known tellurium line directly, an offset lock to a second diode laser, which is stabilized to a tellurium line, can be used for laser frequency stabilization. Alternatively, a locking scheme based on a frequency-stabilized transfer cavity (see, e.g., [53]) can

be implemented. By a controlled variation of the cavity length, a frequency tuning over the full mode-hop-free tuning range is accessible [54]. In this case, tellurium spectroscopy can be used for frequency calibration with respect to a known tellurium line. Alternatively, a frequency comb may be used for improved absolute frequency calibration.

The lifetime of the optical transition shown in Fig. 2 at 441.3 nm is 9.57 ms [24], such that from a single ion a fluorescence emission rate of about 50 s^{-1} is expected at saturation. The laser intensity needed for saturation of the closed-cycle transition is about 75 nW cm^{-2} for a narrowband laser. With an assumed linewidth of the excitation laser of about 1 MHz, a laser intensity of a few mW cm^{-2} and a total power of about 1 mW are needed to saturate the optical transitions. This power is readily available from our diode laser system (see above). The required power for the microwave excitation of the Zeeman transitions at 65 and 130 GHz is estimated to be of order $10 \mu\text{W}$ and is also available with our 10 mW microwave source, which is frequency stabilized to a 10 MHz external rubidium clock with a relative accuracy on the 100 s scale of order 10^{-12} .

The overall detection efficiency including solid angle, light transmission of the different optical elements, and the quantum efficiency of a channel photon multiplier (CPM) detector is estimated to be about 2%. Hence, for a cloud of 10^5 stored ions, the photon count rate is expected to be of order 10^4 s^{-1} , which allows a good signal-to-noise ratio for the optical detection.

D. Precision and benefits

For an evaluation of the measured Zeeman splittings, the magnetic field strength B at the position of the ion has to be determined with high accuracy. This is achieved via the free cyclotron frequency ω_c of a single ion with known mass m and use of the relation $\omega_c = qB/m$, where q is the ion charge. Following the “invariance theorem” [55], the free cyclotron frequency is given as the squared sum of all three ion oscillation frequencies. To that end, it is required to measure the reduced cyclotron frequency ω_+ , the axial oscillation frequency ω_z , and the magnetron drift frequency ω_- by electronic pickup as described in detail, for example, in [50,56]. For single ions, such measurements have been performed in numerous variations including also coupling of individual motions, which reach accuracies of ppb and better [57–59]. In principle, on this level of accuracy, measurements are susceptible to charge effects [60]. However, for a single ion in our trap, space charge effects are absent and image charge effects can well be corrected for.

The precision of g_J values is then limited by the magnetic field measurement and stability, which are typically in the ppb regime within the usual measurement times. In the case of boronlike argon, the upper-level Larmor frequency sets a comparable limit by its natural width. The Zeeman splitting in longer-lived states, however, can be determined with the significantly higher accuracy of microwave and rf technology. The present system involves two different g_J factors. The relation of simultaneously measured Larmor frequencies may profit from this: In general, one g_J factor may be used as reference for the other instead of the cyclotron frequency.

This is of particular interest because of the following physical motivation: The leading-order value of most g_J factors is a rational number given by the Landé formula for coupling of spin and orbital moments. For instance, in a P doublet, the lower and upper levels have $g_{1/2} = 2/3$ and $g_{3/2} = 4/3$, respectively. Deviations from the ratio of exactly 2 are of purely relativistic and quantum-electrodynamical origin, as discussed in Sec. II. They usually do not scale with the same rational factor; hence they are not canceled, but refined from the trivial offset, by the arithmetic operation $g' = g_{3/2} - 2g_{1/2}$. This small difference can be measured more directly by modulation of the fundamental microwave oscillation with a finite radio frequency instead of generating the radiation with two separate microwave synthesizers. Carrier and sidebands will be mixed in the up-conversion process and the frequency interval, as defined by the modulation, is conserved. Then both Zeeman transitions are driven simultaneously with a single source, and the refined value g' is derived from the radio frequency with its attendant precision. This removes the uncertainty due to cancellation of two microwave frequencies.

The deviation of this radio frequency from zero reflects the deviation of the actual g_J factors from the Landé formula and allows determination of the anomalous contributions without the precision restriction caused by the cyclotron frequency.

V. SUMMARY AND OUTLOOK

We have shown that an understanding of the Zeeman effect at higher orders also is indispensable for spectroscopy of highly charged ions at the current level of experimental precision. We have provided a detailed calculation of the first-, second-, and third-order Zeeman effects for a boronlike system as presently under investigation. Experimental schemes for the separation of the respective contributions to the Zeeman effect have been given, together with a description of the corresponding experimental setup for in-trap laser-microwave double-resonance spectroscopy of confined, highly charged ions. Such measurements yield well-defined access to higher-order Zeeman effects in highly charged ions.

ACKNOWLEDGMENTS

This work has been supported in part by DFG (Grants No. VO 1707/1-2 and No. BI 647/4-1) and GSI. D.A.G., A.V.V., M.M.S., V.M.S., and G.P. received support from a grant of the President of the Russian Federation (Grant No. MK-3215.2011.2), by RFBR (Grants No. 12-02-31803 and No. 10-02-00450), and by the Ministry of Education and Science of Russian Federation. D.A.G. acknowledges support by the FAIR-Russia Research Center, and by the “Dynasty” Foundation. D.L. is supported by IMPRS-QD Heidelberg.

-
- [1] F. A. Jenkins and E. Segré, *Phys. Rev.* **55**, 52 (1939).
 - [2] L. I. Schiff and H. Snyder, *Phys. Rev.* **55**, 59 (1939).
 - [3] W. R. S. Garton and F. S. Tomkins, *Astrophys. J.* **158**, 839 (1969).
 - [4] G. Feinberg, A. Rich, and J. Sucher, *Phys. Rev. A* **41**, 3478 (1990).
 - [5] M. Raoult, S. Guizard, D. Gauyacq, and A. Matzkin, *J. Phys. B* **38**, 171 (2005).
 - [6] K. Numazaki, H. Imai, and A. Morinaga, *Phys. Rev. A* **81**, 032124 (2010).
 - [7] G. W. Preston, *Astrophys. J.* **160**, L143 (1970).
 - [8] T. Hamada, *Publ. Astron. Soc. Jap.* **23**, 271 (1971).
 - [9] S. B. Kemic, *Astrophys. Space Sci.* **36**, 459 (1974).
 - [10] R. Williams and A. Mason, *Rev. Mex. Astron. Astrofiz., Ser. Conf.* **26**, 33 (2006).
 - [11] C. Moran, T. R. Marsh, and V. S. Dhillon, *Mon. Not. R. Astron. Soc.* **299**, 218 (1998).
 - [12] H. F. Beyer and V. P. Shevelko, *Introduction to the Physics of Highly Charged Ions*, Series in Atomic and Molecular Physics (Institute of Physics, London, 2002).
 - [13] H. F. Beyer and V. P. Shevelko, *Atomic Physics with Heavy Ions*, Springer Series on Atoms and Plasmas Vol. 26 (Springer, Heidelberg, 1999).
 - [14] M. Vogel and W. Quint, *Phys. Rep.* **490**, 1 (2010).
 - [15] W. Quint, D. L. Moskovkhin, V. M. Shabaev, and M. Vogel, *Phys. Rev. A* **78**, 032517 (2008).
 - [16] D. von Lindenfels, N. Brantjes, G. Birkel, W. Quint, V. Shabaev, and M. Vogel, *Can. J. Phys.* **89**, 79 (2011).
 - [17] V. A. Yerokhin, K. Pachucki, Z. Harman, and C. H. Keitel, *Phys. Rev. Lett.* **107**, 043004 (2011).
 - [18] H.-J. Kluge *et al.*, *Adv. Quantum Chem.* **53**, 83 (2008).
 - [19] I. Draganić, J. R. Crespo López-Urrutia, R. DuBois, S. Fritzsche, V. M. Shabaev, R. Soria Orts, I. I. Tupitsyn, Y. Zou, and J. Ullrich, *Phys. Rev. Lett.* **91**, 183001 (2003).
 - [20] A. N. Artemyev, V. M. Shabaev, I. I. Tupitsyn, G. Plunien, and V. A. Yerokhin, *Phys. Rev. Lett.* **98**, 173004 (2007).
 - [21] R. Soria Orts, J. R. Crespo López-Urrutia, H. Bruhns, A. J. González Martínez, Z. Harman, U. D. Jentschura, C. H. Keitel, A. Lapierre, H. Tawara, I. I. Tupitsyn, J. Ullrich, and A. V. Volotka, *Phys. Rev. A* **76**, 052501 (2007).
 - [22] V. Mäckel, R. Klawitter, G. Brenner, J. R. Crespo López-Urrutia, and J. Ullrich, *Phys. Rev. Lett.* **107**, 143002 (2011).
 - [23] I. I. Tupitsyn, A. V. Volotka, D. A. Glazov, V. M. Shabaev, G. Plunien, J. R. Crespo López-Urrutia, A. Lapierre, and J. Ullrich, *Phys. Rev. A* **72**, 062503 (2005).
 - [24] A. Lapierre, U. D. Jentschura, J. R. Crespo López-Urrutia, J. Braun, G. Brenner, H. Bruhns, D. Fischer, A. J. González Martínez, Z. Harman, W. R. Johnson, C. H. Keitel, V. Mironov, C. J. Osborne, G. Sikler, R. Soria Orts, V. Shabaev, H. Tawara, I. I. Tupitsyn, J. Ullrich, and A. Volotka, *Phys. Rev. Lett.* **95**, 183001 (2005).
 - [25] A. V. Volotka, D. A. Glazov, G. Plunien, V. M. Shabaev, and I. I. Tupitsyn, *Eur. Phys. J. D* **38**, 293 (2006).
 - [26] A. V. Volotka, D. A. Glazov, G. Plunien, V. M. Shabaev, and I. I. Tupitsyn, *Eur. Phys. J. D* **48**, 167 (2008).
 - [27] D. A. Glazov, A. V. Volotka, A. A. Schepetnov, M. M. Sokolov, V. M. Shabaev, I. I. Tupitsyn, and G. Plunien, *Phys. Scr.* (to be published).
 - [28] S. Sturm, A. Wagner, B. Schabinger, J. Zatorski, Z. Harman, W. Quint, G. Werth, C. H. Keitel, and K. Blaum, *Phys. Rev. Lett.* **107**, 023002 (2011).

- [29] A. Wagner, S. Sturm, F. Köhler, D. A. Glazov, A. V. Volotka, G. Plunien, W. Quint, G. Werth, V. M. Shabaev, and K. Blaum, *Phys. Rev. Lett.* **110**, 033003 (2013).
- [30] V. M. Shabaev, I. I. Tupitsyn, V. A. Yerokhin, G. Plunien, and G. Soff, *Phys. Rev. Lett.* **93**, 130405 (2004).
- [31] J. Sapirstein and W. R. Johnson, *J. Phys. B* **29**, 5213 (1996).
- [32] R. Cowan, *The Theory of Atomic Spectra* (University of California Press, Berkeley, CA, 1981).
- [33] J. Sapirstein and K. T. Cheng, *Phys. Rev. A* **66**, 042501 (2002).
- [34] D. A. Glazov, A. V. Volotka, V. M. Shabaev, I. I. Tupitsyn, and G. Plunien, *Phys. Lett. A* **357**, 330 (2006).
- [35] A. V. Volotka, D. A. Glazov, I. I. Tupitsyn, N. S. Oreshkina, G. Plunien, and V. M. Shabaev, *Phys. Rev. A* **78**, 062507 (2008).
- [36] I. I. Tupitsyn (unpublished).
- [37] F. Arbes, M. Benzing, Th. Gudjons, F. Kurth, and G. Werth, *Z. Phys. D* **31**, 27 (1994).
- [38] A. Munch, M. Berkler, Ch. Gerz, D. Wilsdorf, and G. Werth, *Phys. Rev. A* **35**, 4147 (1987).
- [39] F. Arbes, O. Becker, H. Knab, K. H. Knoll, and G. Werth, *Nucl. Instrum. Methods Phys. Res. B* **70**, 494 (1992).
- [40] W. Demtröder, *Laserspektroskopie* (Springer, Berlin, 1993).
- [41] D. von Lindenfels, Diploma thesis, University of Heidelberg, 2010), <http://www.gsi.de/documents/DOC-2011-Feb-63-1.pdf>
- [42] H. Häffner, T. Beier, S. Djekić, N. Hermanspahn, H.-J. Kluge, W. Quint, S. Stahl, J. Verdú, T. Valenzuela, and G. Werth, *Eur. Phys. J. D* **22**, 163 (2003).
- [43] L. S. Brown and G. Gabrielse, *Rev. Mod. Phys.* **58**, 233 (1986).
- [44] G. Gabrielse, L. Haarsma, and S. L. Rolston, *Int. J. Mass Spectrom. Ion Process.* **88**, 319 (1989).
- [45] F. G. Major, V. N. Gheorghe, and G. Werth, *Charged Particle Traps* (Springer, Berlin, 2004).
- [46] S. Djekic, J. Alonso, H.-J. Kluge, W. Quint, S. Stahl, T. Valenzuela, J. Verdú, M. Vogel, and G. Werth, *Eur. Phys. J. D* **31**, 451 (2004).
- [47] M. Vogel, W. Quint, and W. Nörtershäuser, *Sensors* **10**, 2169 (2010).
- [48] A. G. Marshall, C. L. Hendrickson, and G. S. Jackson, *Mass Spectrom. Rev.* **17**, 1 (1998).
- [49] S. Guan and A. G. Marshall, *Anal. Chem.* **65**, 1288 (1993).
- [50] D. J. Wineland and H. G. Dehmelt, *J. Appl. Phys.* **46**, 919 (1975).
- [51] S. Bharadia, M. Vogel, D. M. Segal, and R. C. Thompson, *Appl. Phys. B: Lasers Opt.* **107**, 1105 (2012).
- [52] J. Cariou, and P. Luc, *Atlas du Spectre d'Absorption de la Molécule Tellure* (CNRS Laboratoire Aime-Cotton, Paris, 1980).
- [53] S. Albrecht, S. Altenburg, C. Siegel, N. Herschbach, and G. Birkel, *Appl. Phys. B: Lasers Opt.* **107**, 1069 (2012).
- [54] S. Albrecht, H. Jestädt, and G. Birkel, Absolute frequency measurements on $^{130}\text{Te}^2$ reference lines around 488 nm, in preparation (2013).
- [55] L. S. Brown and G. Gabrielse, *Phys. Rev. A* **25**, 2423 (1982).
- [56] L. Gruber, J. P. Holder, and D. Schneider, *Phys. Scr.* **71**, 60 (2005).
- [57] K. Blaum, *Phys. Rep.* **425**, 1 (2006).
- [58] S. Ulmer, K. Blaum, H. Kracke, A. Mooser, W. Quint, C. C. Rodegheri, and J. Walz, *Phys. Rev. Lett.* **107**, 103002 (2011).
- [59] S. Sturm, A. Wagner, B. Schabinger, and K. Blaum, *Phys. Rev. Lett.* **107**, 143003 (2011).
- [60] D. F. A. Winters, M. Vogel, D. M. Segal, and R. C. Thompson, *J. Phys. B* **39**, 3131 (2006).